Supplementary Information

Field-Programmable Robotic Folding Sheet

Hyunkyu Park[1†], Yongrok Jeong[2†], Woojong Kim[1], Jungrak Choi[3], Junseong Ahn[4], Jun-Ho Jeong[5], Inkyu Park[1*], Jung Kim[1*]

[1] Department of Mechanical Engineering, Korea Advanced Institute of Science and Technology, Daejeon 34141, Republic of Korea

[2] School of Mechanical Engineering, Kyungpook National University, Daegu 41566, Republic of Korea

[3] Electronics and Telecommunications Research Institute (ETRI), Daejeon 34129, Republic of Korea

[4] Department of Control and Instrumentation Engineering, Korea University, Sejong 30019, Republic of Korea

[5] Korea Institute of Machinery and Materials (KIMM), Daejeon 34103, Republic of Korea

† These authors contributed equally

* Corresponding author email: jungkim, inkyu@kaist.ac.kr

This Supplementary Information includes:

Supplementary Notes 1 to 9
Supplementary Figures 1 to 27
Supplementary Table 1 to 3
Supplementary References

Further Supplementary Materials:

Supplementary Movies 1 to 6 (.mp4)

Supplementary Notes

Supplementary Note 1: Details in previous works and contribution of our work

Recent advancements in shape transformation technology aim to achieve a complicated and reconfigurable shape morphing mechanism[1–7]. To this end, robotic folding has long been of great importance for managing extensive design space while endowing many promising functionalities, such as structural compliance against various environments and versatilities in operation[8–12]. Folding has been demonstrated in two concepts[13]: origami, the art of paper folding, and local bending, as exemplified by foldable displays. In origami folding, the crease structure can achieve a large morphing range and enrich the assorted shape configurations in a straightforward manner, by means of a planar figure. For instance, the close-packable Li-ion battery[14], the transformable wheel[15,] and the reliable soft pneumatic actuator[16] were achieved by the Miura-ori pattern, the waterbomb pattern, and the Yoshimura pattern, respectively. Active and delicate control of the folding process can then be realized by part-by-part addressing of each hinge deformation[17–28]. However, predetermination in the hinge designs may restrict the enrichment of accessible shape configurations. A high-density arrangement of unit hinges and actuation parts would serve a definite solution to this challenge. In this regard, the overall folding process becomes a recruitment of a set of sub-hinge segments. This approach has been demonstrated through manual hinge actuator relocation on 4×4 arrangements of two right isosceles triangle tiles[29], or magneto-optical Kerr effect hysteresis loops-based repetitive and independent magnetization of composing elements[30], but relies on in-plant hardware retreatments that restrict exterior uses. A modular assembly of the motorized triangular tiles serves the dynamical control of two-dimensional folding[31], demonstrating shape reconfiguration at once, spanning multiple robotic applications. While such shape morphing systems can showcase a large range of morphing around the domain (able to fully fold/unfold), the structural compartments exhibit a limited density in hinge lines.

Therefore, the reconfiguration of hinge itself, in terms of the location, orientation, and number, holds future possibilities for dynamical shape-reprogramming process, but the most of these are hard to be reconfigured on-the-fly. Folding by local bending[32–49] constitutes a compelling solution, where the hinge can now be freely defined by an unbounded selection along the continuous domain. In terms of hinge reconfiguration, reprogramming of folds by in-plant rectification has been presented, involving retreatment of the local crosslinking state of polymers that are stimuli-responsive by light[36], chemicals[50], and scar pattern[51], or the refinement in the alignment direction of magnetic particles[52–54]. Beyond these previous attempts, we aim to achieve dynamic, in-situ programming of the fold, which we call as field-programming of folds. In general, field-programmable shape-morphing systems have been proposed by adopting spatiotemporally addressable control methods to a distributed hardware design performing local elevation/drop (see Supplementary Table 1 for comparison between previous spatiotemporally addressable control methods). Pixelating the distributed stimuli injection is the most straightforward method to realize. For instance, direct addressing allows for the maximal degree of freedom (DOF) in control, but requires a high number of independent control sources[55,56]. In contrast, matrix addressing can provide a balance in DOF and the number of control sources, offering efficiency in overall control logic[57]. However, the difficulty in building hardware with dense control units restricts the enrichment of DOF. In addition, inefficiencies in increasing DOF exist as current shape responses of the materials are bounded by an unsatisfactory curvature limit. For instance, given a fixed size of the overall domain, further discretization does not guarantee a better number of shape outcomes with the same degree of shape changes, because the shape change density remains the same. Therefore, a networked design has been proposed as a compelling alternative. For instance, the networked design of hardware, driven by periphery electrodal stimulation (e.g., 4 electrical current sources control a 3×3 grid[58], 8 electrical current sources control a 4×4 grid[59], and 32 electrical current sources control an 8×8 grid[60]), allows for higher DOF in reconfigurable shapes with the same number of control units compared to pixelation, because the approach further accounts for the interdependency among the control units.

Despite their significant advancements, no studies have yet reported achieving field-programming of folding, and attempting to use the method for autonomous robot operations. To this end, we have stated four key requirements to realize folding as outlined in the introduction:

(i) The hinge should be digitally reconfigurable with densely distributed stimulation segments, with sufficient spatial resolution and number of degrees of freedom in shape-programming process. This is because the folding is highly narrowed deformation process. In addition, the degrees of freedom should be realized with a minimal number of control units, to achieve simplicity in hardware construction and efficiency in control sources. Therefore, we propose an addressing method well-suited for folding, involving an 8×8 grid electrodes and a centered square lattice network of actuation segments (resistors in our work). Such the design is thoroughly compared with the rest of the addressing schemes in theoretical aspects, as shown in Supplementary Fig. 1 and Supplementary Note 3. As a result, we achieved high flexibility in folding reconfiguration, for instance, being able to induce 29 single diagonal folding lines

(Fig. 1c(i) and Supplementary Movie 1), or folding angles finer than principal lines (vertical/horizontal/diagonals) (Fig. 1c(iii) and Supplementary Movie 1).

(ii) The shape change, curvature inducement in folding, should be continuously maneuverable with a sufficient range of shape change, at least ranging folding angles from -90 ° to 90 °. To this end, we tailored the material structure to fold, by endowing inextensibility to preserve zero Gaussian curvature (which serves as a substantial basis for folding in theory), and free end in the boundary. In addition, we improved the stimuli-responsiveness compared to the monolithic material design (Supplementary Fig. 3), and carefully tuned the size of actuation segments (setting the distance between electrodes of 9 mm in this work).

(iii) The morphing mechanism should avoid extrinsic driving principles that confine operations to fixed workspaces. Many field-programmable shape-morphing systems have demonstrated intricate shape changes, envisioning next-generation meta-surfaces, but require stationing. Regarding robotic deployments, we aimed to field-program the folding by an intrinsic driving principle for exterior uses, designed to be operated through electrical wires and embeddable electronics.

(iv) The internal sensing modality is demanded to drive state to servo, accelerate, and robustify the shape-programming process. The regime serves as a substantial basis for reliable operation under unstructured environmental conditions. In line with requirement (iii), the sensing mechanism should also rely on the intrinsic driving principle toward autonomous operation outdoors. To this end, we implemented sensing modality (temperature distribution) of the internal control state (heat inducement), with no further complication of the hardware structure.

Supplementary Note 2: Details on the selection of driving principle

Shape-morphing mechanisms have leveraged various external stimuli, such as magnetic[61–66], electrical[67–69], optical[70,71], chemical [72–74], hygroscopic[75–79], and fluidic[80–83] mechanisms, offering flexibility in their selection upon environmental characteristics, dynamic responsiveness, geometrical scale, energy density, and distinctive functionalities[84–88]. From these respected previous attempts, a selection of the electrical driving principle for our field-programmable robotic sheet was proceeded to adhere to our four key requirements. As noted in Supplementary Note 1, spatial localizability in stimulation is substantial to induce folding by local bending, which thereby leads chemical and hygroscopic principles unfavorable. While magnetic and optical principles can manage rich shape-morphing configurations, their control sources require fixation of material location confined to indoor workspaces, as the material response is highly sensitive to the direction of source injection from the exterior. Therefore, fluidic and electrical principles, which are intrinsically driven by direct physical connections, are compelling options for autonomous deployment. Realization by the fluidic principle would definitely assure high energy density and large deformation, but is highly challenging to recruit a large number of control units, 64 in our work, due to the bulkiness of each control switch (that is, valve for them). In contrast, electrical principles can simply rely on digital switches, which are highly compact and embeddable in many robotic systems. Moreover, an internal sensing modality can be easily implemented, by monitoring electrical properties such as resistance[89].

Electrical methods can be subdivided into four categories: electrothermal actuators, piezoelectric actuators, ion polymer metal composite (IPMC) actuators, and dielectric elastomer actuators (DEA)[90,91]. While all the approaches have shown fine curvature responses, we selected electrothermal actuation, owing to the high linearity and reliability in stimuli-to-curvature relationship, toward reliable maneuvering of shape; the use of IPMC is challenged by the offset drift due to the evaporation of internal liquids[92,93], and DEA and piezoelectric actuators exhibit nonlinear[34,94–97], or hysteretic responses[98,99], complicating reliable closed-loop control. Among the various materials for electrothermal actuation, a bi-morph structure[67,100,101] meets the aforementioned requirements. The bi-morph structure refers to the layering of two materials with different coefficients of thermal expansion (CTE), managing curvature change through structural deformation, rather than material characteristics. In contrast, liquid crystal elastomer (LCE)[102,103] exhibits nonlinearity[102,104,105], and shape-memory materials (shape-memory polymers[106–108], shape-memory alloys[109–111]) displays hysteretic responses against temperature[112–114].

Supplementary Note 3: Details of networked resistor design

As described in the manuscript, the functional basis was constructed in the 7×7 grid arrangement of a centered square lattice toward a high spatial resolution in accessible shape configuration, with electrodes placed in every corner of the lattice as 8×8 grids. In line with the reconfigurability of the heating pattern, the spatial uniformity in heating should be additionally considered. To this end, the geometry of the metal serpentine was carefully tailored upon the following equations. Given the area *A* filled with metal resistor pathway with constant pitch (*p*), width (*w*), and thickness (*t*), the resistance of the resistor is derived as

$$R = \rho \frac{l}{wt} = \rho \frac{\frac{A}{p}}{wt} = \rho \frac{A}{wtp}, \quad \text{(S1)}$$

where ρ is resistivity of the metal. From the equation, we can conclude that R is linearly proportional to *A*. For the heating case involving a single vertical / horizontal line at the sheet (Supplementary Fig. 27), the areal geometry of the resistors, that are horizontal / vertical (*hv*) or diagonal (*d*), was tailored to achieve a spatially uniform heating which is equivalent to the electrical power density (*E' = E/A*, where *E* is the total electrical power at each resistor). The related formulation governs the relationship among the geometry of the two types of the resistor, as

$$E' = \frac{E}{A} = \frac{\frac{4V^2}{R_{hv}}}{A_{hv}} = \frac{4V^2}{kA_{hv}^2} = \frac{\frac{V^2}{R_d}}{A_d} = \frac{V^2}{kA_d^2}, \quad \text{(S2)}$$

$$A_{hv} = 2A_d\ , \quad \text{(S3)}$$

where *V* is the voltage imposed to the resistor and *k* is $\frac{\rho}{wtp}$. The compartment of the resistors was performed to meet the condition of (S3) while assuring the full occupancy of the surface, resulting in the design as Supplementary Fig. 2.

Supplementary Note 4: Details of fabrication procedure and conditions

On the 4” Silicon (Si) wafer (Supplementary Fig. 6a), Polyimide (PI) varnish (PI-1388; Vtec, USA) was spin coated (2000 rpm, 30s), soft baked (150 ºC, 1 min) and imidized (260 °C, 1 hr) to form the PI layer for substrate (Supplementary Fig. 6b). On the substrate PI layer, serpentine-shaped networked resistor was patterned by conventional lithography process (MDA-400M-6; MIDAS System, South Korea), following to the design in Supplementary Note 3 (Supplementary Fig. 7a). For lithography, photoresist (PR) (AZ5214E; MicroChemicals GmbH, Germany) was spin coated (2000 rpm, 30s), soft baked (112.5 °C, 1 min), exposed (~40 mJ/cm^2), post-exposure baked (122.5 °C, 2 min), flood exposed (~500 mJ/cm^2), and developed (1 min) with compatible developer (AZ300MIF; Merck, Germany), to achieve the negative tone of pattern via reversal bake process of the AZ5214E. Sequentially, Chrome (Cr) and Nickel (Ni) was deposited by E-beam deposition (DKEB-02-04; Daeki Hi-tech, South Korea), with thickness of 3 nm and 150 nm, respectively, and with deposition speed of 5 Å/s for both materials. After deposition, pattern was lift-offed by Acetone (Supplementary Fig. 6c). Onto the Cr/Ni networked resistor, the Cr/Al etch stop layer was additionally deposited by shadow mask deposition, with design of Supplementary Fig. 7b (Supplementary Fig. 6d). The overall networked resistor-patterned film was covered with the additional PI layer that formed by spin coating (3000 rpm, 30 s), soft baking (150 °C, 1 min) and imidization (260 °C, 1 hr), for insulation and protection of networked resistor from external environment (Supplementary Fig. 6e).

Toward connection of the substrate with electronics, via hole at insulating PI layer should be formed. Since dry etch of the PI is the most effective method for precise etching, hard mask of Al, with thickness of 100 nm, was patterned by lift-off process similar with abovementioned procedure (Supplementary Fig. 6f), following design of Supplementary Fig. 7c. PI via hole was formed by reactive ion etching (RIE) process (SRN-300; SORONA, South Korea) by applying Al hard mask layer and underneath Al layer as etch stop layer. RIE was conducted for 25 min, with condition as follows: gas flow of 100 sccm of O_2 and 20 sccm of CF_4, plasma power of 100 W, and working pressure of 200 mTorr (Supplementary Fig. 6g). After PI via-hole formation, Al hard mask was selectively etched by diluted buffered oxide etchant (BOE) in DI (deionized) water, with volume ratio of 1:5 (Supplementary Fig. 6h). Since it is well known that Ni have bad wettability with solder, additional solder wetting layer (Cr/Cu/Au, 30 /1000 /30 [nm]) was E-beam deposited and patterned by shadow mask following design in Supplementary Fig. 7d (Supplementary Fig. 6i). The diameter of solder wetting layer was larger than via hole, and thus cover the overall via. This intended to prevent the possible torn of the via hole, which composed of the thinner PI layer.

Next, SU-8 microrod was patterned by the lithography process. To form the SU-8 microrod with designed thickness (150 μm), SU-8 50 (Kayaku advanced materials, USA) was selected and spin coated with speed of 2000 rpm, for 30 s. Coated SU-8 was soft baked (67.5 °C, 20 min / 97.5 °C, 50 min), exposed (250 mJ/cm^2) in periodic dot pattern (d = 50 μm, p = 75 μm), post-exposure baked (97.5 ºC, 12 min), and developed (SU-8 developer and isopropyl alcohol (IPA), 5 min of developing & IPA cleaning, for 4 times). Afterward, formed SU-8 microrod were hard-baked (200 ºC, 30 min) (Supplementary Fig. 6j). In sequence, cream solder (SAC305) was applied on the solder wetting layer by cream solder dispenser (YDL-983A; LY, China, 5 atm of dispensing pressure and 0.3s of dispensing time), and solder pad was formed by soldering them on hot plate (250 ºC, 2 min) (Supplementary Fig. 6k). Next, PDMS (Sylgard 184; Dow corning, USA, 10:1 mixing ratio) was spin coated (1000 rpm, 30 s) and vacuum processed (10 min) to uniformly and certainly soak the PDMS in between the SU-8 microrod pattern (Supplementary Fig. 6l). After vacuum process, additional PDMS was spin coated (3000 rpm, 30 s) to control the thickness of the PDMS layer (Supplementary Fig. 6m). Coated PDMS was cured on hot plate, with various curing temperature depends on purpose (60 ºC ~ 150 ºC). The SEM image of cross-sectional view for fabricated shape morphing structures can be found in Supplementary Fig. 8.

Before the electrical connection, coated PDMS over via was scraped by knife, while underneath networked resistor layer was protected by solder pad (Supplementary Fig. 6n). Next, overall sheet was delaminated from Si wafer by soaked into the deionized water (DI water) (Supplementary Fig. 6o). Enameled ultrathin Copper (Cu) wire with diameter of 50 μm (45 AWG), which was picked to minimize the possible physical disturbance by wire, was soldered onto the sheet, by cold-soldering iron with temperature of 250 ºC, to avoid the damage of fabricated sheet (Supplementary Fig. 6p).

Supplementary Note 5: Comparison in specification with previous researches

This note introduces the comparative evaluation of shape-morphing performance among existing polymer-based electrothermal actuators, including our work. Among the similar ratio of coefficient of thermal expansion (CTE) between strain-inducing and strain-limiting layers (<10), the performance was benchmarked in terms of the curvature range, time constant, and the material structure. The following are the detailed description on each regime.

1) Curvature range (cm^{-1}): Curvature range determines the shape-morphing performance, that is the difference among the maximum and minimum of curvature.
2) Time constant (s): Time constant represents the dynamical responsiveness of the shape change. In general, the value is the time takes for the system to reach a certain faction (usually, 63.2 %) of its steady-state value.
3) Material structure: Many attempts exist to modulate the directionality of thermal expansion in the strain-inducing layer, by using composite material design. 'Monolithic' stands for using the homogeneous material, 'Unidirectional lamella (UL)' orients the structural thermo-responsiveness along the single direction (e.g., microwall pattern), while 'unidirectional fiber reinforced composite (UFRC)' restricts the thermo-responsiveness along the out-of-plane direction so that the lateral thermal expansions are boosted (e.g., microrod pattern as in our work). Supplementary Fig. 10a displays the schematic illustration of the material structures.

Supplementary Fig. 10b and Supplementary Table 2 present the result of comparison. Our robotic sheet presents a well-balanced performance in the curvature range and time constant. Notably, it is obvious that UL-based ETAs can outperform our work, as the attempts are intended to maximize the unidirectional bending, while our work balances the bending in two dimensions along the material surface.

Supplementary Note 6: Distributional variance analysis

The proposed network-based control method is designed as a promising candidate for the conventional pixelation approaches. A comparative quantitative analysis on the effectiveness of the network method was performed by investigating possible variance of the output distribution. Given n number of grid electrodes that are regularly distributed in a square domain, thereby having a square number, and k number of nonzero voltage magnitudes imposed to the electrodes, both methods have $(2k+1)^n$ cases in voltage distribution, when accounting for the directionality in the voltage values. The number of unique power distributions for the point control method ($\mathcal{N}_{pixel}$) is computed as

$$\mathcal{N}_{pixel}(n,k) = (k+1)^n \,. \qquad \text{(S4)}$$

In case of the network-based method, there exist multiple voltage configurations that result in an identical power distribution. As the simplest instance, any set of voltage configurations consisting of two discrete values can share the same power distribution with configurations in which those values are interchanged or uniformly shifted. The duplication can occur upto $2(2k+1)$ times, depending on the network structure and the shape of output. Therefore, there exists a lower bound on the distributional variance of the network control $\mathcal{N}_{network}$, which can be expressed using big- Ω notation as

$$\mathcal{N}_{network}(n,k) = \Omega\left\{\frac{(2k+1)^n}{2(2k+1)}\right\} = \Omega\left\{\frac{(2k+1)^{n-1}}{2}\right\}. \qquad \text{(S5)}$$

We note that this approach is a conservative setting that facilitates the intuitive characterization by avoiding the highly complex calculation on the exact number of cases. Supplementary Fig. 23 depicts the result of the distribution variance according to the range of n and k. The network control method displays its outperformance in terms of the variability in configuring power distribution compared to the pixelation.

Supplementary Note 7: Numerical algorithms for comparison in distributed actuation

In order to evaluate the computational performance in using Genetic algorithm for the inverse problem in distributed actuation, two numerical optimization methods are established for comparison (i) Linear pseudoinverse method displays the nonlinearity in the governing inverse map. Given $\mathbf{E} \in \mathbb{R}^N$ and $\mathbf{V} \in \mathbb{R}^M$, electrical power distribution and electrodal voltage, respectively, with the number of resistors *N* and number of electrodes *M*, the computation inverts their forward relationship as $\mathbf{V} = \mathbf{G}^{+}\mathbf{E}$, where $\mathbf{G} \in \mathbb{R}^{N\times M}$ is the Jacobian matrix and $(\cdot)^{+}$ is a pseudoinverse operator. (ii) Levenberg–Marquardt iterates the solution by damped gradient update, adhering to the cost function same as the one used for Genetic algorithm. The damping factor is set as 1e-2 until the termination determined by tolerance 1e-8. The discretization of voltage value is performed post-computation.

Supplementary Note 8: RNI drive pattern

A specification in RNI measurements involves not only the number of electrodes and their location, but also a way of selecting electrode pairs for current injection and voltage measurement, which refer to drive pattern, that strongly influences the overall sensing performance. As mentioned in Methods, the design of drive pattern serves as a substantial specification of RNI measurements, in terms of both the reconstruction accuracy and frame rate. Toward computational efficiency, the drive pattern was specifically designed by the following guideline. We first simplified the electrode pair selections as adjacent, due to the large number of electrodes. All the adjacent pair-wise current injection was leveraged to access entire regions of domain. Given each current injection, the electrode pair selections for voltage measurement was reduced by the spatial sensitivity investigation. A spatial sensitivity ($\delta\mathbf{V}/\delta R$) presented here is defined as a ratio of voltage changes ($\delta\mathbf{V}$) with respect to the single resistor change (δR) where the current is injected through the ends of it. The associated voltage measurement was proceeded with all the set of adjacent electrodal pairs. The result of inspection indicates that the voltage measurements sharing the electrode with the current injection exhibits high sensitivity (Supplementary Fig. 25a). From this observation, the drive pattern recruits the specific electrode pairs for voltage measurement adhering to the above condition (Supplementary Fig. 25b). As a result, total 1,470 voltage measurements take place for each RNI sensing.

Supplementary Note 9: Numerical RNI reconstruction methods.

Following the number of methods in generic tomographic problems including EIT, two numerical approaches are established and are compared to the proposing deep-learning-based reconstruction: (i) One-step Gaussian Newton method (GN) is a linear inverse model that can be expressed as $\delta\widehat{\mathbf{R}} = \mathbf{J}^{+}\delta\mathbf{V}$, where $\widehat{\mathbf{R}}$ is the reconstructed resistance and $\mathbf{J} = \frac{\partial\mathbf{V}}{\partial\mathbf{R}} \in \mathbb{R}^{N\times M}$ is Jacobian matrix. We note that $\mathbf{J}$ in RNI is well-posed due to the low complexity in the resistor connections so that it offers an adequate robustness in matrix inversion. (ii) Since the inverse map is intrinsically nonlinear, iterative reconstruction (Iterative GN) is provides better accuracy, at the cost of slow inference speed, as

$$\delta\widehat{\mathbf{R}}_i = \delta\widehat{\mathbf{R}}_{i-1} + \left(\mathbf{J}_i^T\mathbf{J}_i + \lambda^2\mathrm{diag}(\mathbf{J}_i^T\mathbf{J}_i)\right)^{-1}\mathbf{J}_i^T\left(\mathbf{V} - \mathrm{F}(\mathbf{R}_{i-1})\right), \tag{S5}$$

where i is the iteration number, damping hyperparameter (λ) of 4e-10, and the iteration repeats toward the convergence with repetitive update of Jacobian matrix ($\mathbf{J}_i$) with respect to the best reconstructed resistance result.

Supplementary Figures

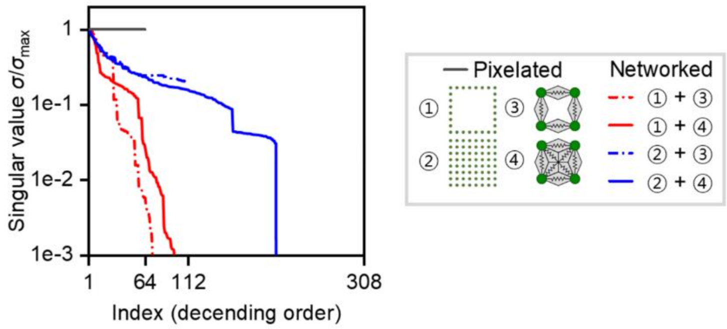

Supplementary Fig. 1. Singular value analysis of the resistor network. The result of singular value analysis. The inset shows the schematic illustration of the configurations in the networked domain (The green circle and gray square represent the electrode, and resistor, respectively). The singular value σ is normalized using the maximum singular value σ_{max}. The singular values out of range drop significantly below 10^{-10}.

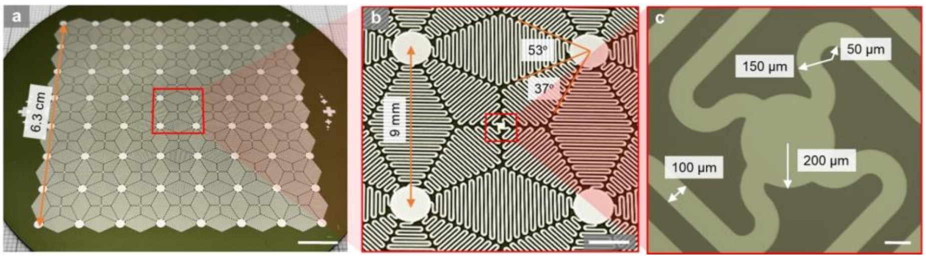

Supplementary Fig. 2. Description of the networked resistor. a-c, Photograph of the networked resistor imaged by an optical camera (**a, b**) and microscope (**c**). The actual wire connection is made at a large circular junction (d = 2 mm), where the small circular junction (d = 0.4 mm) is part of the resistive network, designed as a crossover point among resistors. Scale bars: 9 mm (**a**), 2 mm (**b**), 100 µm (**c**).

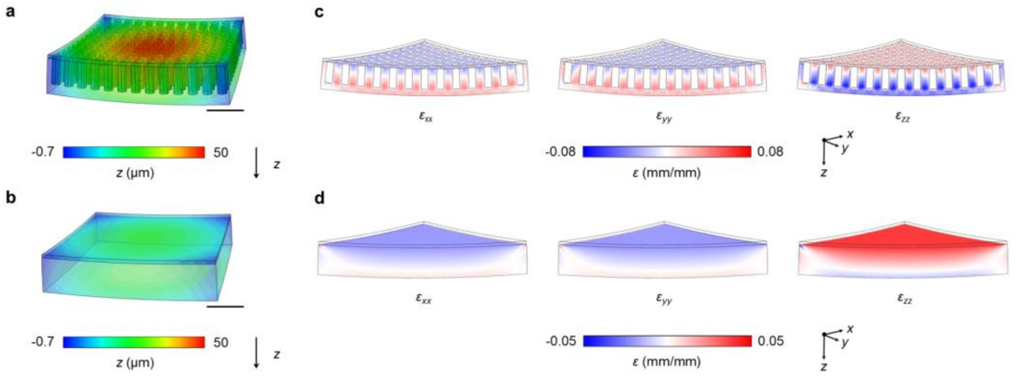

Supplementary Fig. 3. Numerical simulation of the shape-morphing structure. a, **b**, Microscopic FEA prediction of thermomechanical deformation in a miniature cell (occupying area of 975 µm × 975 µm) of the microstructured structure (**a**) and a monolithic structure (**b**). Scale bars, 200 µm. **c**, **d**, Strain distribution (ε_{xx}, ε_{yy}, ε_{zz}) of the microstructured structure (**c**) and a monolithic structure (**d**), sectioned to display internal features.

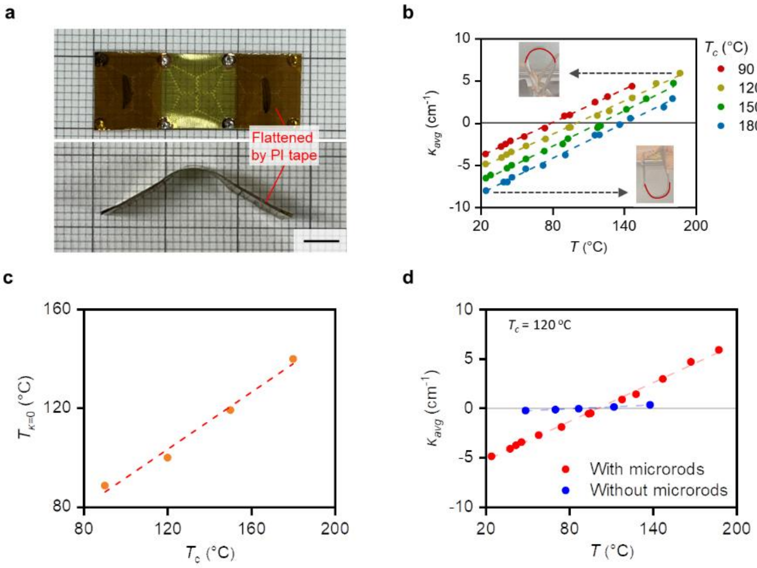

Supplementary Fig. 4. Experimental validation of folding in a tapered specimen. a, Optical images (top and side views) of the tapered specimen used in the experiment. A high aspect ratio in the geometry (3:1 length to width) and flattening at the end ensures one-dimensional folding. Scale bars, 5 mm. **b**, Curvature response to temperature T, at various curing temperature T_c. Averaged value of curvature along the deformed curve, κ_{avg}, is measured. The dashed lines indicate a linear fit ($R^2 > 0.99$). The insets show photographs of the shape changes of the specimen, along with the traced contours (straight red line). It is noteworthy that the mechanical constraints and fully uniform heating amplify the fold when compared with the complete robotic sheet operation. **c**, The relationship between T_c and structural neutralization temperature $T_{\kappa=0}$. The dashed line indicates the linear fit ($R^2 >$ 0.97). **d**, The comparison in curvature response between samples with and without microrod structuring.

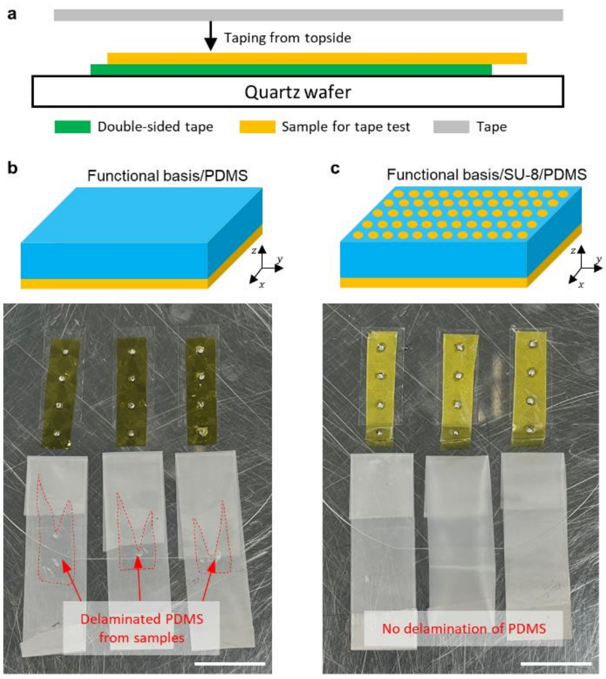

Supplementary Fig. 5. Comparison of adhesion between cases with and without SU-8 microrods. a, Cross-sectional view of experiments. The sample was fixed by double-sided tape (Scotch double-sided tape 137D, 3M, USA) on the quartz wafer. A second tape (Scotch magic tape 810D, 3M, USA) was applied and removed to test the adhesion between the layers of the sample. Two conditions (without and with SU-8 layers) were tested, with three samples each. **b**, Experimental result for the sample without SU-8 microrods. Although the solder pad caused the PDMS layer to tear during tape detachment, all samples showed delamination of the PDMS from the functional basis. Scale bar, 2 cm. **c**, Experimental result for the sample with SU-8 microrods. None of the samples showed PDMS delamination. Scale bar, 2 cm.

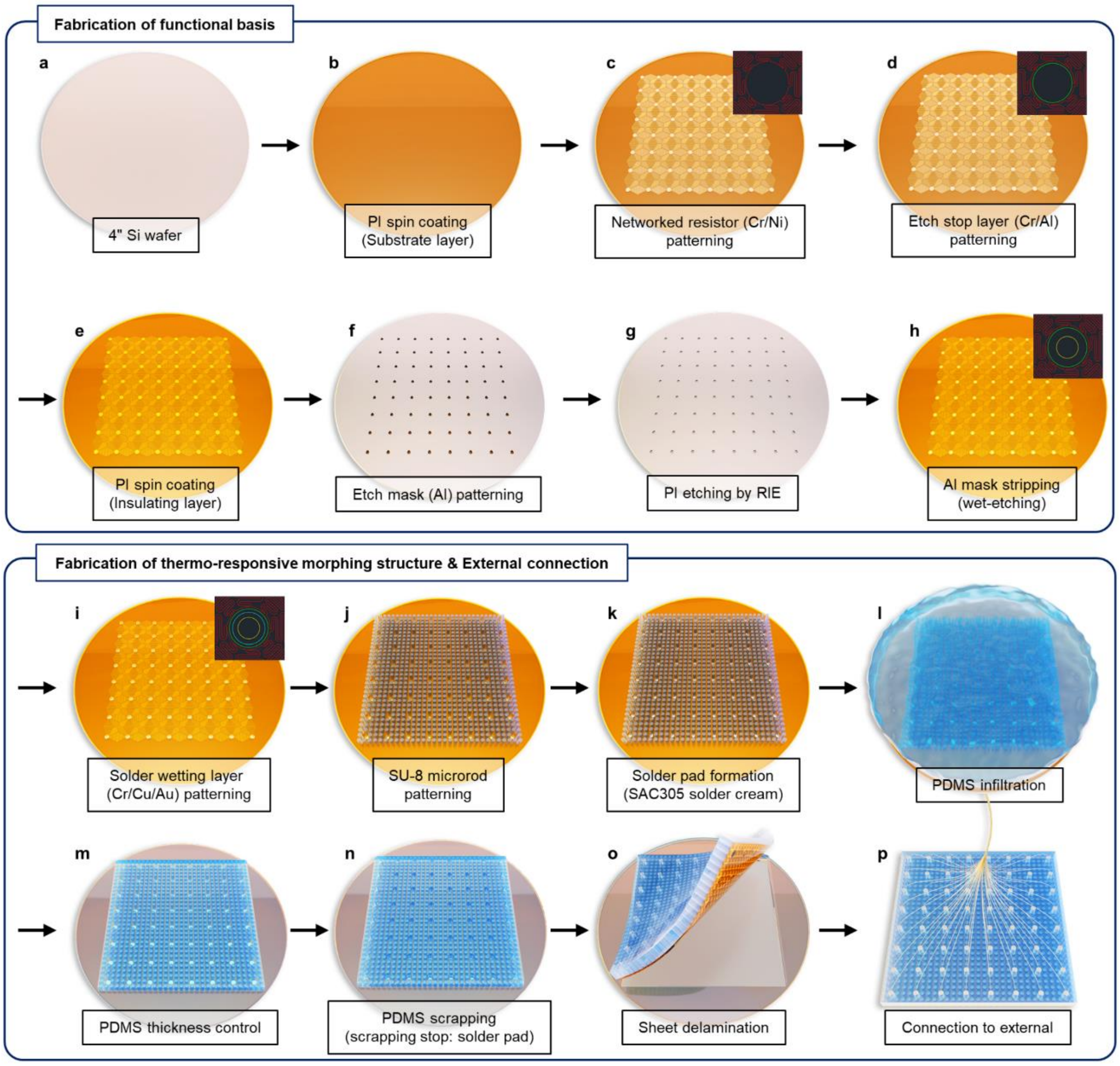

Supplementary Fig. 6. Flowchart of the fabrication. The fabrication begins with the functional basis formation. Upper right inset images show the top-view of via hole patterning process (**a**-**h**). **a,** As-prepared silicon wafer. **b,** Spin coating of polyimide (PI) film. **c,** Networked resistor (Cr 3 nm/Ni 150 nm) patterning by lift-off. **d,** Lower etch stop layer (Cr/Al) patterning by shadow mask. **e,** Spin coating of PI film. **f,** Upper etch stop layer (Al) patterning by lift-off. **g,** PI etching by reactive ion etching (RIE), with etch stop layer of upper and lower Al layer. **h,** Al etch stop layer stripping by wet-etching. Onto the functional basis, the thermo-responsive morphing structure was formed and connected with externals (**i**-**p**). **i,** Solder wetting layer (Cr/Cu/Au) patterning by shadow mask. **j,** SU-8 microrod patterning by lithography. **k,** Solder pad formation. **l,** PDMS vacuum infiltration. **m,** PDMS thickness control by spin coating. **n,** PDMS on via scrapping, with scrapping stop of solder pad. **o,** Sheet delamination. **p,** Connection to the external device by soldering.

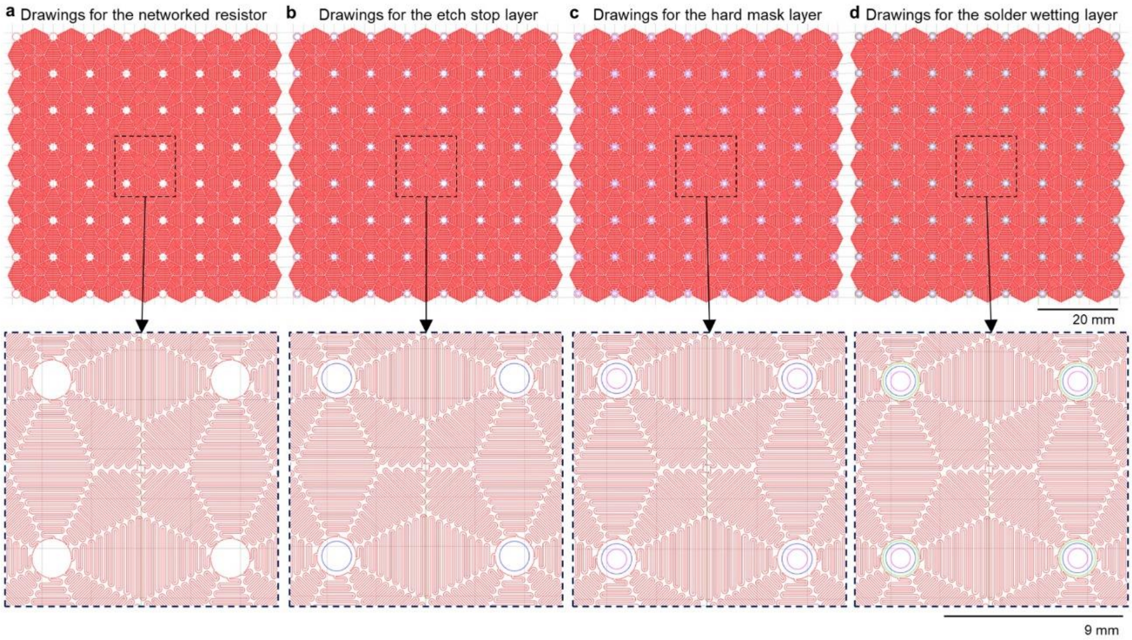

Supplementary Fig. 7. Drawings for the fabrication. a-d, Drawings for the networked resistor (**a**), the etch stop layer (**b**), the hard mask layer (**c**), and the solder wetting layer (**d**).

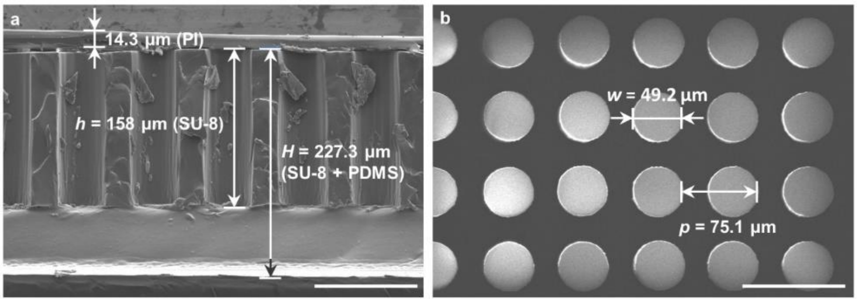

Supplementary Fig. 8. SEM image on the shape-morphing structure. a, Cross-sectional view. Scale bar, 100 μm. **b**, Top view. Scale bar, 100 μm.

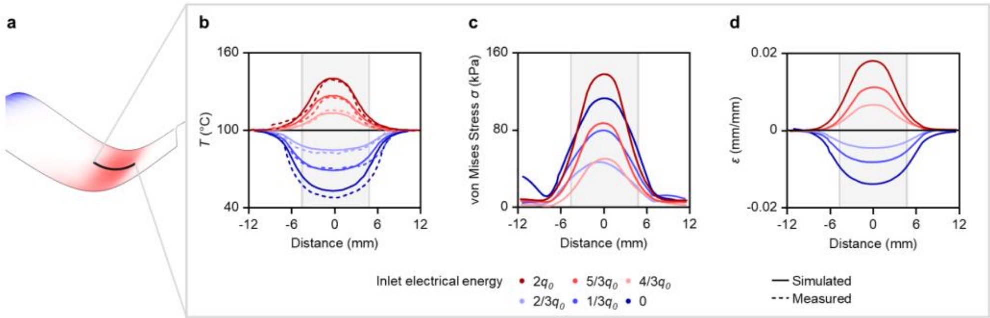

Supplementary Fig. 9. Distributional investigation of multi-physical response from the whole-body scale FEA. a, Schematic illustration of the analysis region. **b-d**, Cross-sectional views of the predicted temperature (**b**), stress (**c**), and strain (**d**) in response to various electrical energy levels proportional to the base energy level for mechanical neutralization q_0. In **b**, the measurement using the IR camera (dashed lines) is in good agreement with the computed value. For **b-d**, the gray box represents the region of activation.

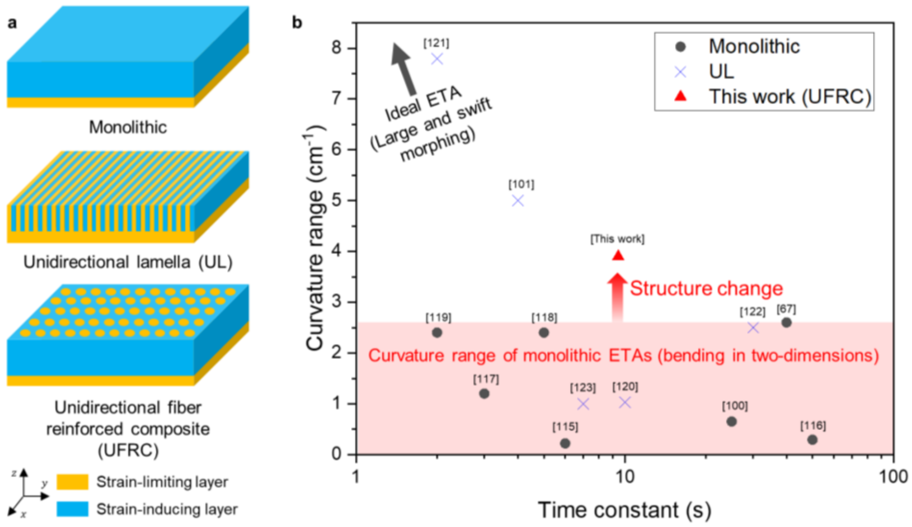

Supplementary Fig. 10. Comparison in curvature range and response time of the proposed electrothermal actuator (ETA) with previously reported ETAs. a, Types of structures for ETA. Conventionally, monolithic and unidirectional lamella (UL) structures were adopted, and this study adopted the unidirectional fiber reinforced composite (UFRC) structure. **b**, Comparison graph of the proposed ETA with the previous researches.

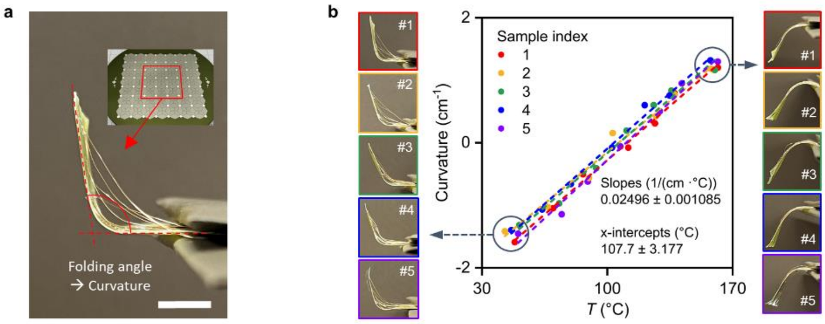

Supplementary Fig. 11. Curvature response along different specimens. a, Five specimens from different fabrication batches were selected and sectioned into 30 mm × 30 mm pieces (4 × 4 electrode arrangement) for comparison. Scale bar, 1 cm. **b**, Comparison between specimens. The slopes show a standard deviation of 4.34 % from their mean value, and x-intercepts show a standard deviation of 2.9 % from their mean value.

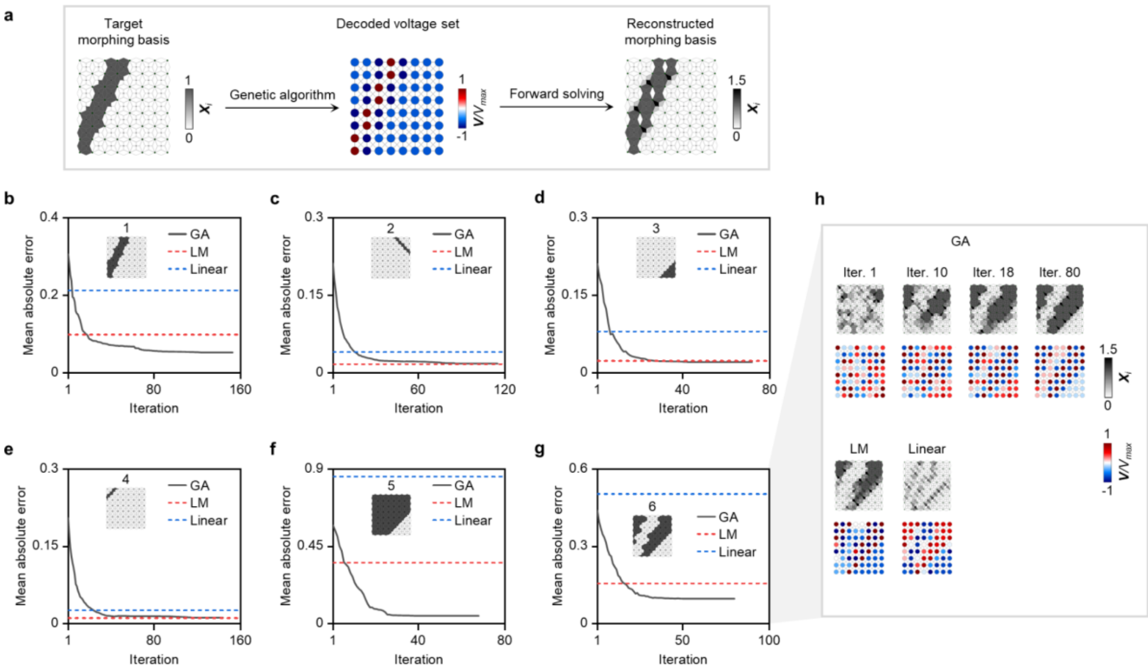

Supplementary Fig. 12. Description and evaluation of distributed actuation. a, Schematic illustration of the solving process for distributed actuation. Morphing basis $\mathbf{X}_i$ is decoded into the set of electrode voltage **V**. The resulting morphing basis can be obtained by forward-solving process using resistive network analysis. **b-g**, Performance evaluation of the algorithm for selected morphing basis. GA and LM refer to genetic algorithm and Levenberg–Marquardt algorithm, respectively. **h**, Visualization of the results of morphing basis reconstruction for the morphing basis used in **g**. Note that the decoded voltage set in the linear method remains continuous to avoid nonlinear processing of the value.

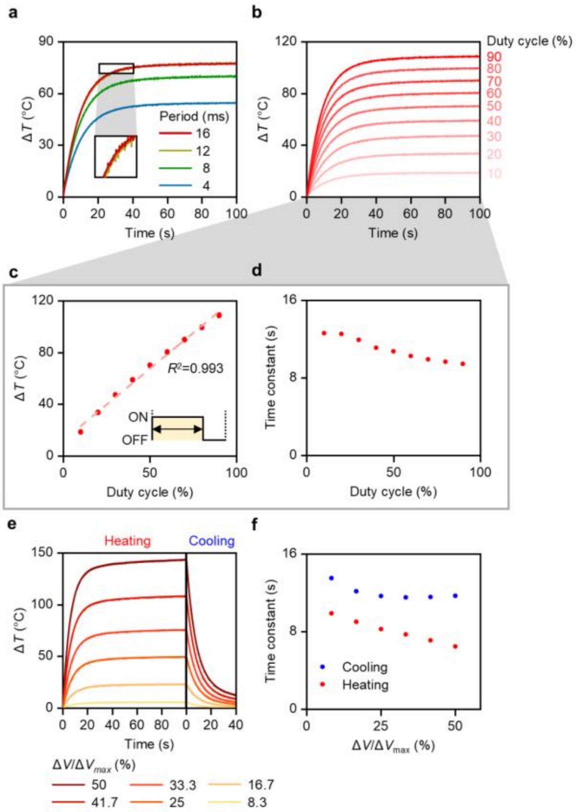

Supplementary Fig. 13. Experimental characterizations on thermodynamics of electrothermal stimulation. a, Effect of time period in PWM on the transient temperature response. The inset shows a negligible difference in the results for periods of 12 and 16 ms. **b**, Temperature response with respect to the change in duty cycle. **c**, Linear relationship between duty cycle and steady-state temperature. The inset shows a schematic illustration of the duty cycle, that is the occupancy of the onset within a fixed time period. **d**, Time constant of the transient response in PWM. **e**, Plain transient temperature response with respect to invariant voltage stimulation ΔV in a ratio to maximum voltage difference ΔV_{max}. Both heating and cooling processes are depicted with a separate temporal evolution. **f**, Time constant of the plain response shown in **e**.

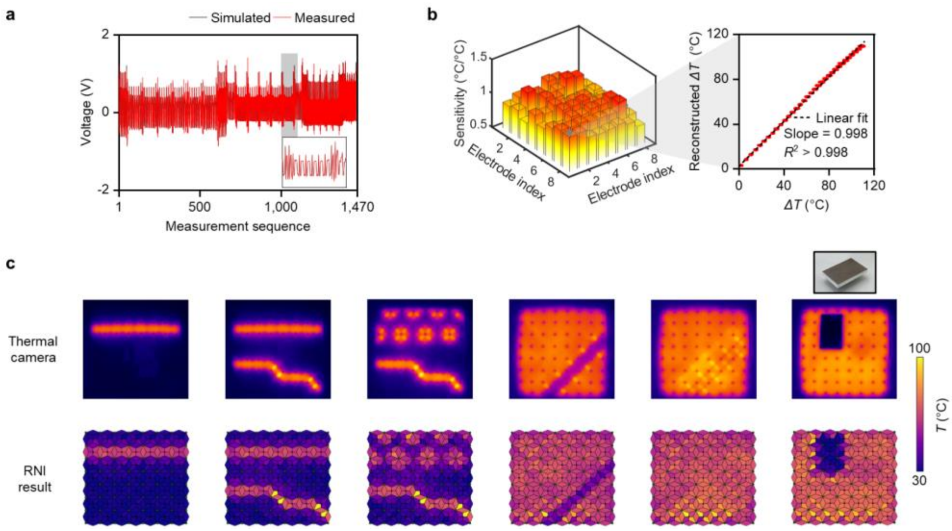

Supplementary Fig. 14. Description and evaluation of Resistive Network Imaging (RNI) method. a, Electrical simulation of the resistive network shows high accuracy of the measurement. The inset shows a detailed comparison of voltage values within the selected range. **b**, Experimental results of spatial uniformity in temperature measurements. Sensitivity of temperature estimation was investigated with respect to heating by imposing voltage changes on a single electrode. The inset shows a sample result of the detailed temperature estimation, which exhibits high linearity. **c,** Demonstration of generalized reconstruction capability, in comparison with thermal camera measurements. In the rightmost case, a small metal block is placed on the sheet to highlight its ability to monitor external disturbances.

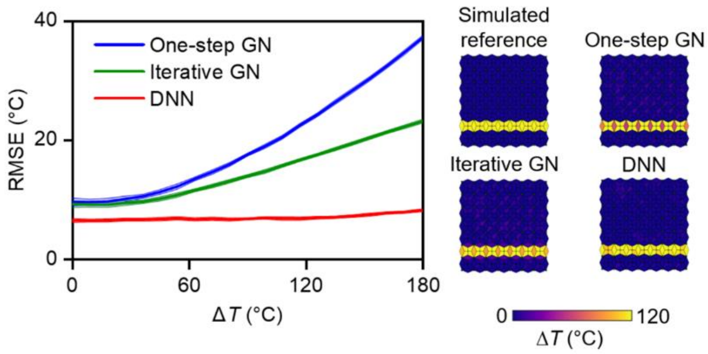

Supplementary Fig. 15. Simulation study on the RNI reconstruction performance. RMSE measurement of the reconstruction error, compared with the numerical approaches. The inset displays a sample result of reconstruction.

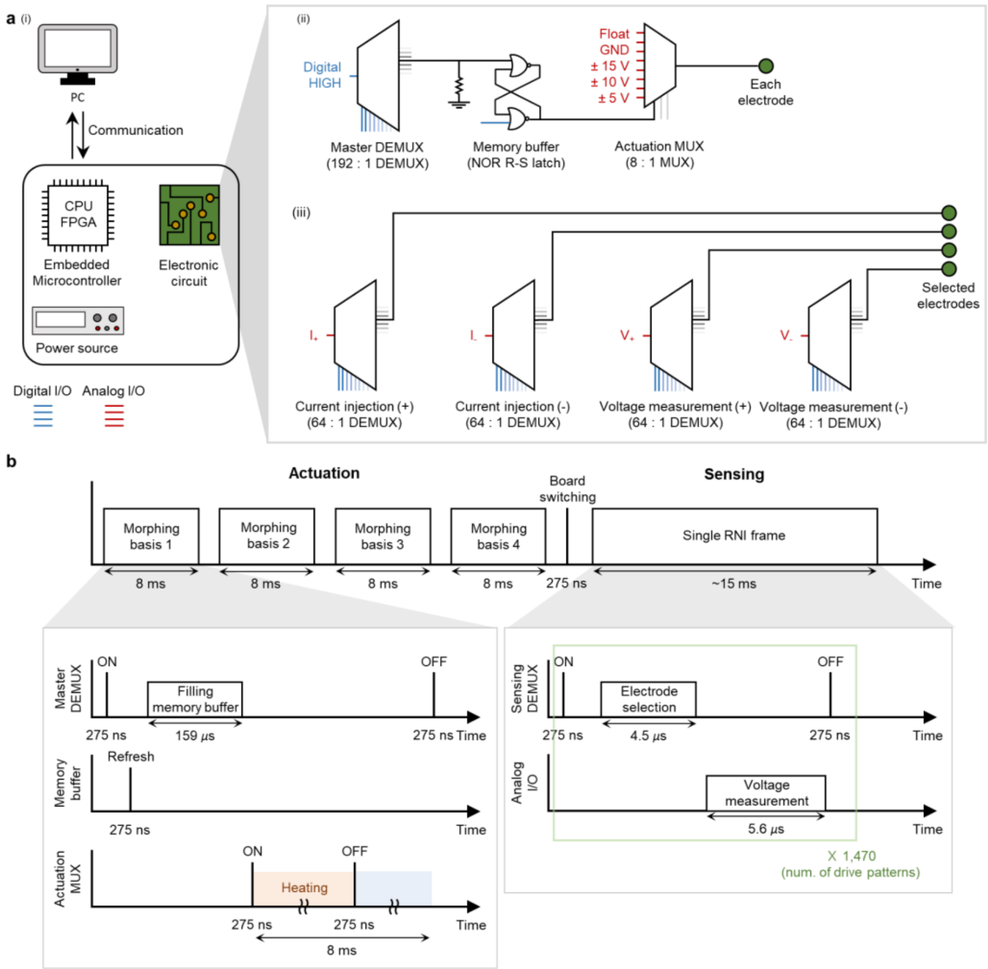

Supplementary Fig. 16. Structure and control strategies of electronics. a, Circuit diagram for driving the robotic folding sheet, which involves high-level controllers (i) and an electrical circuit for actuation (ii) and sensing (iii). **b**, Timing diagram for sequential operation of actuation and sensing.

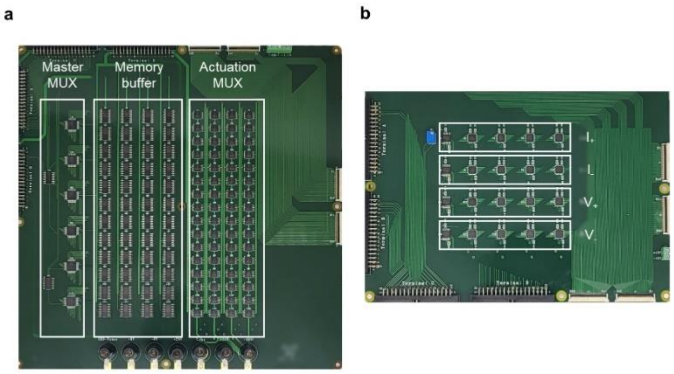

Supplementary Fig. 17. Printed circuit board. a-b, The electronics for actuation (**a**) and sensing (**b**).

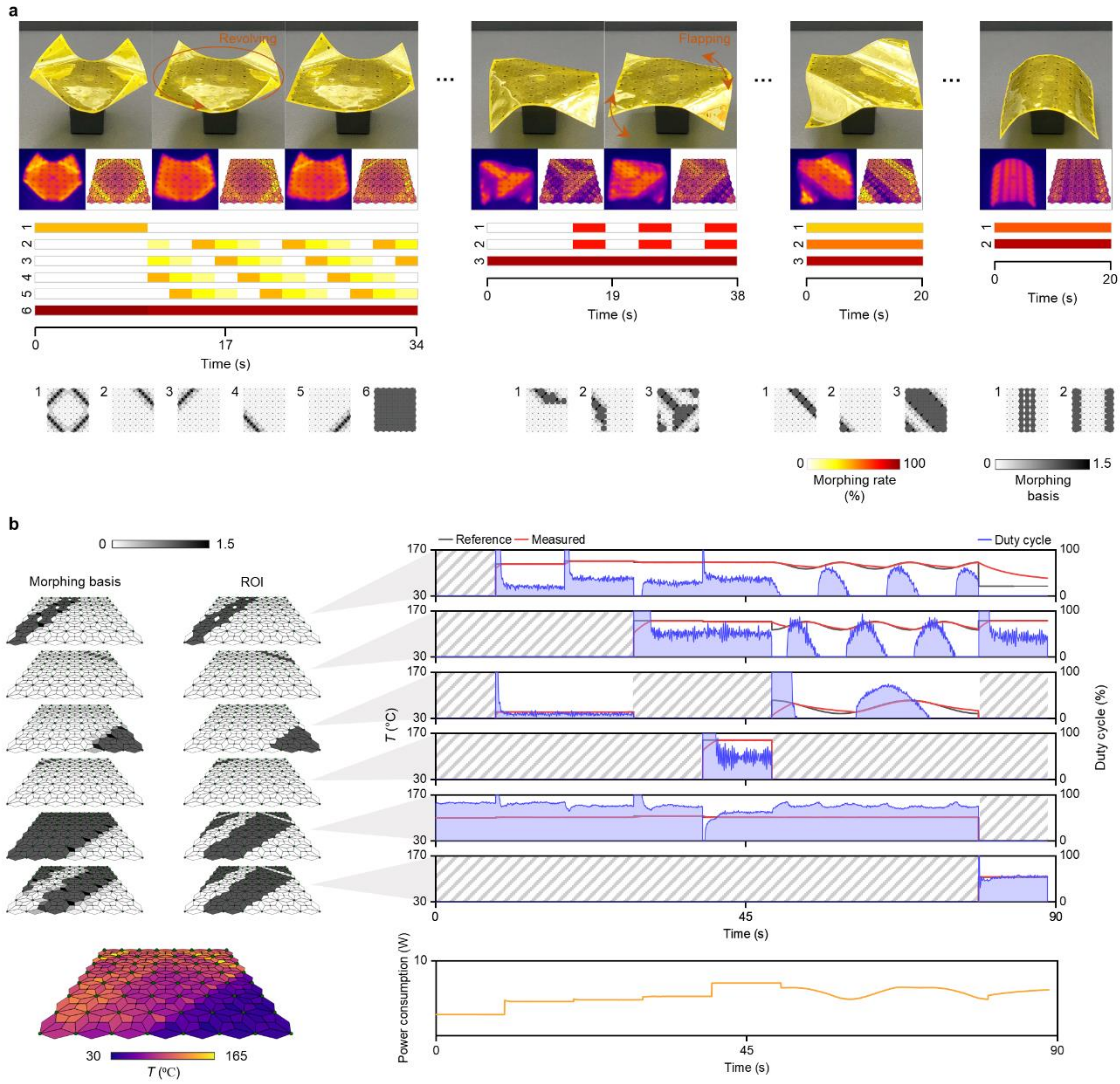

Supplementary Fig. 18. Details in fold-programming process. a, Sequential scheduling of morphing basis recruitment for the remaining morphing scenario shown in Fig. 3d. **b**, Tracking of temperature trajectories and power consumption for each morphing basis recruitment. The left illustration displays the region of interest (ROI) used for segmental temperature measurements.

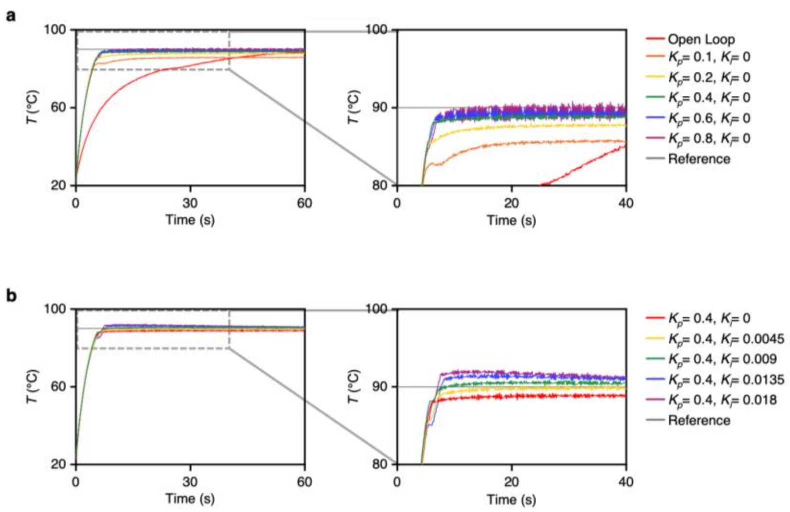

Supplementary Fig. 19. Transient response analysis of the thermodynamics. a, Transient response of open-loop control and P control in electrothermal stimulation. The P gain (K_p) accelerates temperature tracking, but an excessive increase leads to a chattering effect. Based on this observation, the value of K_p was selected as 0.4. The selected P control yields a shorter settling time (5 %) compared to the open-loop control, displaying 6.64 and 44.37 s, respectively. **b**, Transient response with PI control. Given a fixed K_p (=0.4), the I gain (K_i) reduces the steady-state error, but an excessive increase leads to overshoot due to tight saturation of the control input. Based on this observation, the value of K_i was selected as 0.009. The selected PI control exhibits a lower steady state error than the P control, displaying 0.22 and -1.13 °C, respectively.

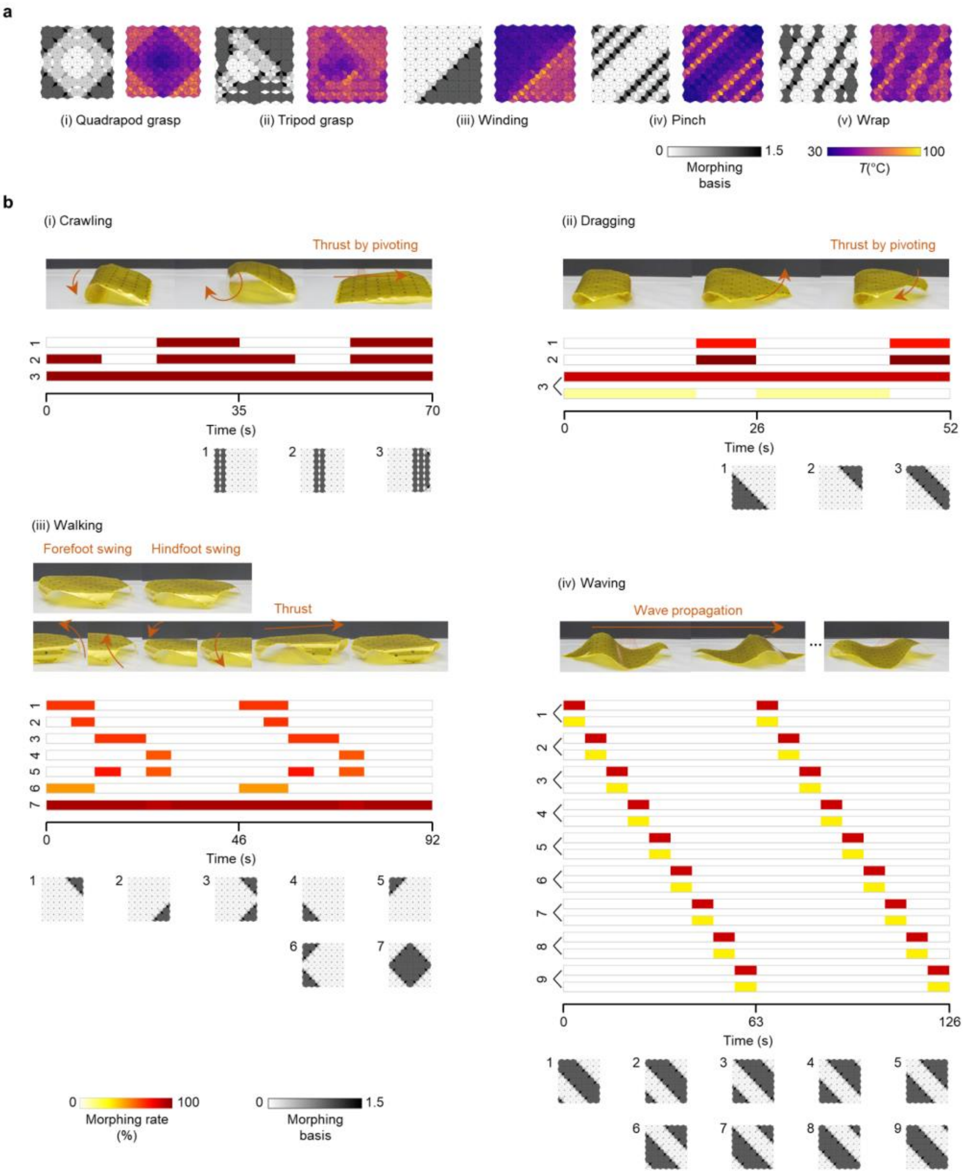

Supplementary Fig. 20. Shape-morphing design for grasping and locomotion applications. a, The morphing basis and RNI temperature measurements for each grasping poses. **b**, Sequential scheduling of morphing basis recruitment for each locomotive strategy.

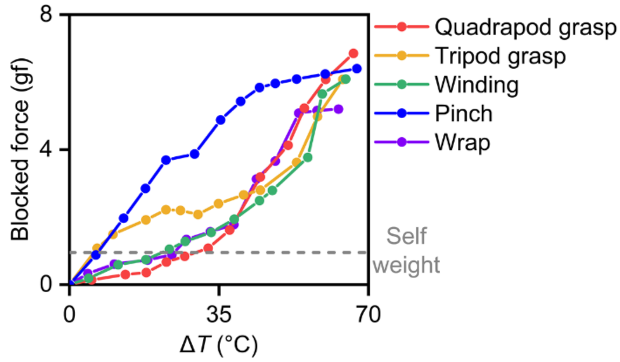

Supplementary Fig. 21. Blocked force during grasping. The blocked force was measured for five different grasping strategies to evaluate the pressure resistance. The results show that the grasping can withstand a force greater than 7 times its own weight.

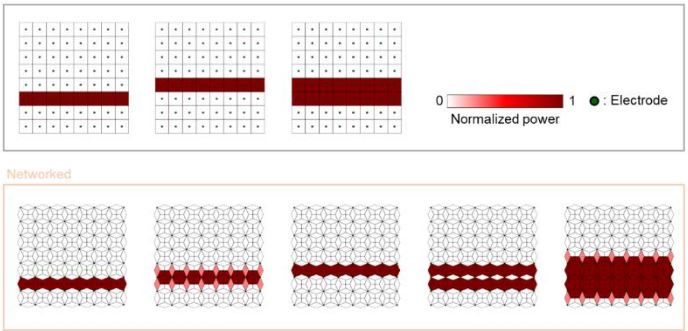

Supplementary Fig. 22. Sample demonstration of line folding scenario. Conceptually, the networked domain can enrich the possible horizontal single line folding, in comparison with the pixelated domain under same electrode configuration (8 × 8).

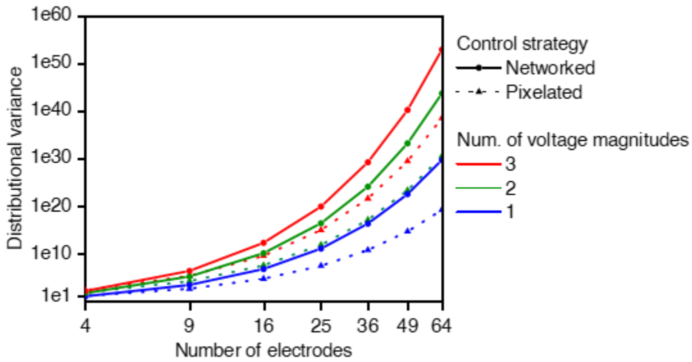

Supplementary Fig. 23. Distributional variance analysis of the resistor network. The number of possible unique power distributions is theoretically computed with respect to the number of electrodes (n) and the number of voltage magnitudes (k).

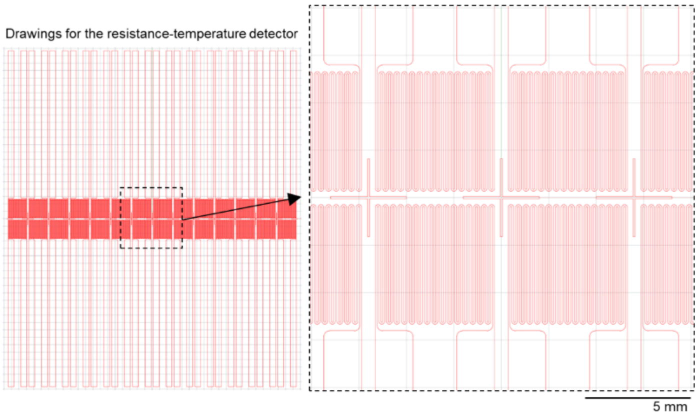

Supplementary Fig. 24. Drawing for the resistance-temperature detector (RTD). As in the design of the networked resistor, the serpentine pattern, comprised of Au (100 nm) and adhesive layer of Cr (3 nm), with pattern width of 100 µm and pitch of 200 µm was fabricated by the lift-off method.

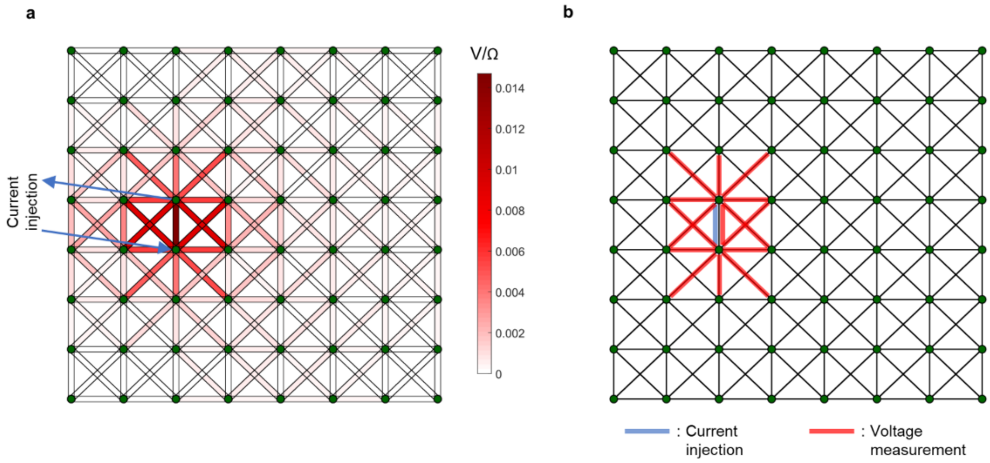

Supplementary Fig. 25. Spatial sensitivity analysis and resulting driving pattern design in RNI. a, A sample result of spatial sensitivity, with respect to the current injection through the selected electrode pair. **b,** The driving pattern obtained from the inspection of (**a**).

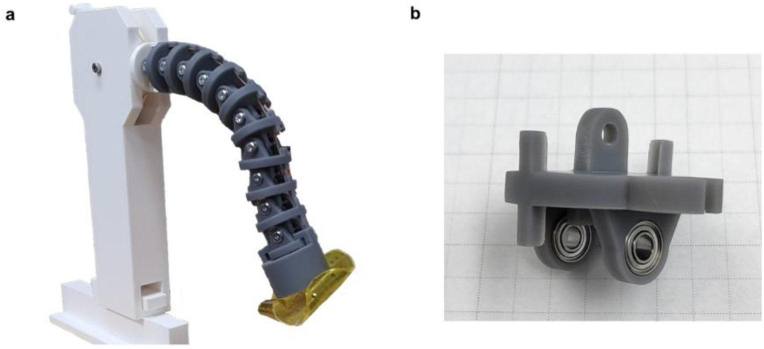

Supplementary Fig. 26. Customized continuum manipulator for grasping application. **a,** A photograph of the continuum manipulator. **b,** An enlarged view of the single joint.

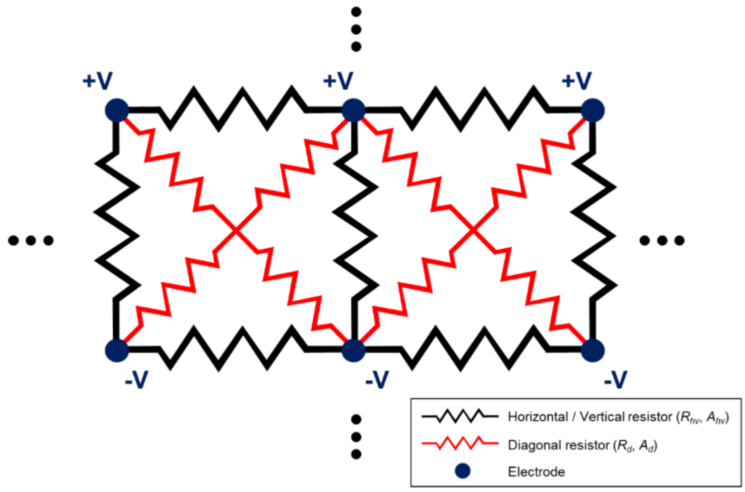

Supplementary Fig. 27. Design scenario for achieving uniform heating with the functional bases. Areal geometry of each type of resistor (placed horizontal / vertical (*hv*), and diagonal (*d*)) was tuned to uniformize the electrical power density of resistors.

Supplementary Tables

Requirements \ Mechanisms	Niu, D. et al.[55]	Johnson, B. K. et al.[56]	Wang, J. et al.[57]	Liu, K. et al.[58]	Ni, X. et al.[59]	Bai, Y. et al.[60]	This work
Domain resolution	4×4 pixels	10×10 Pixels	6×6 pixels	24 networks	40 networks	40 networks	308 networks
Electrode configuration	4×4 grids	10×10 grids	12 boundary connections	6 boundary connections	16 boundary connections	16 boundary connections	8×8 grids
Morphing scheme	Local elevation	Local elevation	Bending	Bending	Local elevation	Local elevation	Folding / bending / rolling
Curvature range (for bending, cm^{-1})	-	-	Middle (-0.4 ~ 0.4)	Low (data N/A)	-	-	High (-1.4~1.3)
Driving principle origination	Extrinsic	Intrinsic	Intrinsic	Intrinsic	Extrinsic	Extrinsic	Intrinsic
Sensing modality	N/A	Internal	N/A	N/A	External (camera)	External (camera)	Internal

Supplementary Table 1. Comparison between present field-programmable elements.

Structure	Curvature range (cm^{-1}).	Time constant (s)	Thickness (μm)
Monolithic[115]	0.074*	12*	770
Monolithic[100]	0.65	25*	560*
Monolithic[116]	0.187*	15*	370
Monolithic[67]	2.6	20*	212.5
Monolithic[117]	1.2	5*	130
Monolithic[118]	2.4	1*	105
Monolithic[119]	2.54	2*	15
UL[101]	5*	3*	115
UL[120]	1.03	6.3*	47
UL[121]	7.8	2*	44
UL[122]	2.5	8*	40
UL[123]	1*	7*	300
UFRC (This work)	3.9	9.454*	240

UL: unidirectional lamella, UFRC: unidirectional fiber reinforced composite

* Asterisked values are estimated from each of the references. Curvature range is estimated following reference[124].

Supplementary Table 2. Details for previously researched electrothermal actuator (ETA). For each case, types of structure, curvature range, time constant, and thicknesses are investigated.

Materials	**PDMS**	**SU-8**	**PDMS-SU-8 composite**	**Ni**[125]	**PI**
Classification	Isotropic	Isotropic	Transversely isotropic	Isotropic	Isotropic
Young's modulus (MPa)	2.46[126]	4,950[127]	E_{xx} = 6.374 E_{yy} = 6.374 E_{zz} = 1,670	207,000	2,550[128]
Poisson ratio	0.496[129]	0.33[130]	ν_{xy} = 0.770 ν_{yz} = 0.0001662 ν_{xz} = 0.0001662	0.31	0.34[131]
Shear modulus * (MPa)	0.82	1,861	G_{xy} = 1.637 G_{yz} = 1.653 G_{xz} = 1.653	79,010	951
Density (kg/m^3)	1,030[132]	1,190[133]	1,084	8,800	1,410[128]
Coefficient of thermal expansion (ppm/K)	340[132]	29.68[134]	α_{xx} = 349.1 α_{yy} = 349.1 α_{zz} = 29.98	13.1	45[128]
Thermal conductivity (W/m·K)	0.27[132]	0.17[134]	0.2363	60.7	0.308[128]
Constant pressure specific heat capacity (J/kg·K)	1,615[135]	1,600[134]	1,609	460	1,090[136]

*Shear modulus (G) for isotropic materials is estimated by $G = \frac{E}{2(1+\nu)}$, where E is Elastic modulus and ν is Poisson ratio.

Supplementary Table 3. Material parameters for the simulations. For the directionality in orthotropy, z direction is normal to the surface of the sheet structure.

Supplementary References

1. Kaspar, C., Ravoo, B. J., van der Wiel, W. G., Wegner, S. V. & Pernice, W. H. P. The rise of intelligent matter. *Nature* **594**, 345–355 (2021).

2. Prabhakar, A. & Murphey, T. Mechanical intelligence for learning embodied sensor-object relationships. *Nat Commun* **13**, 4108 (2022).

3. Gupta, A., Savarese, S., Ganguli, S. & Fei-Fei, L. Embodied intelligence via learning and evolution. *Nat Commun* **12**, 5721 (2021).

4. Sitti, M. Physical intelligence as a new paradigm. *Extreme Mech Lett* **46**, 101340 (2021).

5. Sun, J., Lerner, E., Tighe, B., Middlemist, C. & Zhao, J. Embedded shape morphing for morphologically adaptive robots. *Nat Commun* **14**, 6023 (2023).

6. Cheng, X. *et al.* Programming 3D curved mesosurfaces using microlattice designs. *Science* **379**, 1225–1232 (2023).

7. Sun, X. *et al.* Machine learning-enabled forward prediction and inverse design of 4D-printed active plates. *Nat Commun* **15**, 5509 (2024).

8. Tang, Y. *et al.* Wireless Miniature Magnetic Phase-Change Soft Actuators. *Advanced Materials* **34**, 2204185(2022).

9. Ford, M. J. *et al.* A multifunctional shape-morphing elastomer with liquid metal inclusions. *Proceedings of the National Academy of Sciences* **116**, 21438–21444 (2019).

10. Roh, Y. *et al.* Vital signal sensing and manipulation of a microscale organ with a multifunctional soft gripper. *Sci Robot* **6**, eabi6774 (2021).

11. Rus, D. & Tolley, M. T. Design, fabrication and control of origami robots. *Nat Rev Mater* **3**, 101–112 (2018).

12. Meloni, M. *et al.* Engineering Origami: A Comprehensive Review of Recent Applications, Design Methods, and Tools. *Advanced Science* **8**, 2000636 (2021).

13. Peraza-Hernandez, E. A., Hartl, D. J., Malak Jr, R. J. & Lagoudas, D. C. Origami-inspired active structures: a synthesis and review. *Smart Mater Struct* **23**, 094001 (2014).

14. Song, Z. *et al.* Origami lithium-ion batteries. *Nat Commun* **5**, 3140 (2014).

15. Lee, D.-Y., Kim, J.-K., Sohn, C.-Y., Heo, J.-M. & Cho, K.-J. High–load capacity origami transformable wheel. *Sci Robot* **6**, eabe0201 (2021).

16. Paez, L., Agarwal, G. & Paik, J. Design and Analysis of a Soft Pneumatic Actuator with Origami Shell Reinforcement. *Soft Robot* **3**, 109–119 (2016).

17. Firouzeh, A. & Paik, J. Robogami: A Fully Integrated Low-Profile Robotic Origami. *J*

Mech Robot **7**, 1–8 (2015).

18. Miyashita, S., Guitron, S., Ludersdorfer, M., Sung, C. R. & Rus, D. An untethered miniature origami robot that self-folds, walks, swims, and degrades. in *2015 IEEE International Conference on Robotics and Automation (ICRA)* 1490–1496 (IEEE, 2015). doi:10.1109/ICRA.2015.7139386.

19. Aukes, D. M., Goldberg, B., Cutkosky, M. R. & Wood, R. J. An analytic framework for developing inherently-manufacturable pop-up laminate devices. *Smart Mater Struct* **23**, 094013 (2014).

20. Zhu, Y., Birla, M., Oldham, K. R. & Filipov, E. T. Elastically and Plastically Foldable Electrothermal Micro-Origami for Controllable and Rapid Shape Morphing. *Adv Funct Mater* **30**, 2003741 (2020).

21. Boyvat, M., Koh, J.-S. & Wood, R. J. Addressable wireless actuation for multijoint folding robots and devices. *Sci Robot* **2**, eaan1544 (2017).

22. Zhu, Y. & Filipov, E. T. Rapid multi-physics simulation for electro-thermal origami systems. *Int J Mech Sci* **202–203**, 106537 (2021).

23. Nisser, M. E. W., Felton, S. M., Tolley, M. T., Rubenstein, M. & Wood, R. J. Feedback-controlled self-folding of autonomous robot collectives. in *2016 IEEE/RSJ International Conference on Intelligent Robots and Systems (IROS)* 1254–1261 (IEEE, 2016). doi:10.1109/IROS.2016.7759208.

24. Niiyama, R. *et al.* Pouch motors: Printable soft actuators integrated with computational design. *Soft Robot* **2**, 59–70 (2015).

25. Koh, J. S. & Cho, K. J. Omega-shaped inchworm-inspired crawling robot with large-index-and-pitch (LIP) SMA spring actuators. *IEEE/ASME Transactions on Mechatronics* **18**, 419–429 (2013).

26. Felton, S., Tolley, M., Demaine, E., Rus, D. & Wood, R. A method for building self-folding machines. *Science* **345**, 644–646 (2014).

27. Guseinov, R., McMahan, C., Pérez, J., Daraio, C. & Bickel, B. Programming temporal morphing of self-actuated shells. *Nat Commun* **11**, 237 (2020).

28. Kabutz, H. & Jayaram, K. Design of CLARI: A Miniature Modular Origami Passive Shape-Morphing Robot. *Advanced Intelligent Systems* **5**, 2370057(2023).

29. Hawkes, E. *et al.* Programmable matter by folding. *Proceedings of the National Academy of Sciences* **107**, 12441–12445 (2010).

30. Cui, J. *et al.* Nanomagnetic encoding of shape-morphing micromachines. *Nature* **575**, 164–168 (2019).

31. Belke, C., Holdcroft, K., Sigrist, A. & Paik, J. Morphological flexibility in robotic systems through physical polygon meshing. *Nat Mach Intell* **5**, 1–7 (2023).

32. Ranzani, T., Russo, S., Bartlett, N. W., Wehner, M. & Wood, R. J. Increasing the

Dimensionality of Soft Microstructures through Injection-Induced Self-Folding. *Advanced Materials* **30**, 1802739 (2018).

33. Gu, H. *et al.* Self-folding soft-robotic chains with reconfigurable shapes and functionalities. *Nat Commun* **14**, 1263 (2023).

34. Ahmed, S. *et al.* Multi-Field Responsive Origami Structures: Preliminary Modeling and Experiments. in *Volume 6B: 37th Mechanisms and Robotics Conference* (American Society of Mechanical Engineers, 2013). doi:10.1115/DETC2013-12405.

35. Ryu, J. *et al.* Photo-origami-Bending and folding polymers with light. *Appl Phys Lett* **100**, 161908 (2012).

36. Zhu, C. N. *et al.* Reconstructable Gradient Structures and Reprogrammable 3D Deformations of Hydrogels with Coumarin Units as the Photolabile Crosslinks. *Advanced Materials* **33**, 2008057 (2021).

37. Cao, Y. & Dong, J. Programmable soft electrothermal actuators based on free-form printing of the embedded heater. *Soft Matter* **17**, 2577–2586 (2021).

38. Guo, Q. *et al.* Programmable 3D Self-Folding Structures with Strain Engineering. *Advanced Intelligent Systems* **2**, 2070121 (2020).

39. Huang, Q. *et al.* Solvent Responsive Self-Folding of 3D Photosensitive Graphene Architectures. *Advanced Intelligent Systems* **5**, 2000195 (2023).

40. Salmon, F. *et al.* Modeling the Mechanical Performance of a Foldable Display Panel Bonded by 3M Optically Clear Adhesives. in *Digest of Technical Papers - SID International Symposium* vol. 48 938–941 (John Wiley and Sons Inc, 2017).

41. Lee, J. H. *et al.* Light-driven complex 3D shape morphing of glassy polymers by resolving spatio-temporal stress confliction. *Sci Rep* **10**, 10840 (2020).

42. Liu, Z., Cui, A., Li, J. & Gu, C. Folding 2D Structures into 3D Configurations at the Micro/Nanoscale: Principles, Techniques, and Applications. *Advanced Materials* **31**, 1802211 (2019).

43. Tian, Z. *et al.* Gaussian-preserved, non-volatile shape morphing in three-dimensional microstructures for dual-functional electronic devices. *Nat Commun* **12**, 509 (2021).

44. Zhao, Z. *et al.* Digital printing of shape-morphing natural materials. *Proceedings of the National Academy of Sciences* **118**, e2113715118 (2021).

45. Liu, Y., Shaw, B., Dickey, M. D. & Genzer, J. Sequential self-folding of polymer sheets. *Sci Adv* **3**, e1602417 (2017).

46. Jamal, M., Zarafshar, A. M. & Gracias, D. H. Differentially photo-crosslinked polymers enable self-assembling microfluidics. *Nat Commun* **2**, 527 (2011).

47. Komatsu, R. *et al.* Repeatedly foldable AMOLED display. *J Soc Inf Disp* **23**, 41–49 (2015).

48. Zhang, Y. & Ionov, L. Controllable self-rolling of polyurethane/SiO2 film with differential density. *Eur Polym J* **119**, 32–36 (2019).

49. Shigemune, H., Maeda, S., Hara, Y., Hosoya, N. & Hashimoto, S. Origami Robot: A Self-Folding Paper Robot With an Electrothermal Actuator Created by Printing. *IEEE/ASME Transactions on Mechatronics* **21**, 2746–2754 (2016).

50. Kohlmeyer, R. R. *et al.* Shape-reprogrammable polymers: Encoding, erasing, and re-encoding. *Advanced Materials* **26**, 8114–8119 (2014).

51. Meeussen, A. S. & van Hecke, M. Multistable sheets with rewritable patterns for switchable shape-morphing. *Nature* **621**, 516–520 (2023).

52. Deng, H. *et al.* Laser reprogramming magnetic anisotropy in soft composites for reconfigurable 3D shaping. *Nat Commun* **11**, 6325 (2020).

53. Song, H. *et al.* Reprogrammable Ferromagnetic Domains for Reconfigurable Soft Magnetic Actuators. *Nano Lett* **20**, 5185–5192 (2020).

54. Alapan, Y., Karacakol, A. C., Guzelhan, S. N., Isik, I. & Sitti, M. Reprogrammable shape morphing of magnetic soft machines. *Sci Adv* **6**, eabc6414 (2020).

55. Niu, D. *et al.* Reconfigurable shape-morphing flexible surfaces realized by individually addressable photoactuator arrays. *Smart Mater Struct* **30**, 125032 (2021).

56. Johnson, B. K. *et al.* A multifunctional soft robotic shape display with high-speed actuation, sensing, and control. *Nat Commun* **14**, 4516 (2023).

57. Wang, J., Sotzing, M., Lee, M. & Chortos, A. Passively addressed robotic morphing surface (PARMS) based on machine learning. *Sci Adv* **9**, eadg8019 (2023).

58. Liu, K., Hacker, F. & Daraio, C. Robotic surfaces with reversible, spatiotemporal control for shape morphing and object manipulation. *Sci Robot* **6**, eabf5116 (2021).

59. Ni, X. *et al.* Soft shape-programmable surfaces by fast electromagnetic actuation of liquid metal networks. *Nat Commun* **13**, 5576 (2022).

60. Bai, Y. *et al.* A dynamically reprogrammable surface with self-evolving shape morphing. *Nature* **609**, 701–708 (2022).

61. Kim, Y. & Zhao, X. Magnetic Soft Materials and Robots. *Chem Rev* **122**, 5317–5364 (2022).

62. Kim, Y., Parada, G. A., Liu, S. & Zhao, X. Ferromagnetic soft continuum robots. *Sci Robot* **4**, eaax7329 (2019).

63. Hu, W., Lum, G. Z., Mastrangeli, M. & Sitti, M. Small-scale soft-bodied robot with multimodal locomotion. *Nature* **554**, 81–85 (2018).

64. Kim, Y., Yuk, H., Zhao, R., Chester, S. A. & Zhao, X. Printing ferromagnetic domains for untethered fast-transforming soft materials. *Nature* **558**, 274–279 (2018).

65. Ze, Q. *et al.* Soft robotic origami crawler. *Sci Adv* **8**, eabm7834 (2022).

66. Yi, S. *et al.* High-throughput fabrication of soft magneto-origami machines. *Nat Commun* **13**, 4177 (2022).

67. Yao, S., Cui, J., Cui, Z. & Zhu, Y. Soft electrothermal actuators using silver nanowire heaters. *Nanoscale* **9**, 3797–3805 (2017).

68. Sirbu, I.-D. *et al.* Electrostatic actuators with constant force at low power loss using matched dielectrics. *Nat Electron* **6**, 1–12 (2023).

69. Li, W. *et al.* An on-demand plant-based actuator created using conformable electrodes. *Nat Electron* **4**, 134–142 (2021).

70. Kuenstler, A. S. *et al.* Blueprinting Photothermal Shape-Morphing of Liquid Crystal Elastomers. *Advanced Materials* **32**, 2000609 (2020).

71. Han, B. *et al.* Plasmonic-Assisted Graphene Oxide Artificial Muscles. *Advanced Materials* **31**, 1806386 (2019).

72. Cangialosi, A. *et al.* DNA sequence–directed shape change of photopatterned hydrogels via high-degree swelling. *Science* **357**, 1126–1130 (2017).

73. Wehner, M. *et al.* An integrated design and fabrication strategy for entirely soft, autonomous robots. *Nature* **536**, 451–455 (2016).

74. Jin, D. *et al.* Four-dimensional direct laser writing of reconfigurable compound micromachines. *Materials Today* **32**, 19–25 (2020).

75. Liu, X. *et al.* Recent Advances in Stimuli-Responsive Shape-Morphing Hydrogels. *Adv Funct Mater* **32**, 2203323 (2022).

76. Jiao, D., Zhu, Q. L., Li, C. Y., Zheng, Q. & Wu, Z. L. Programmable Morphing Hydrogels for Soft Actuators and Robots: From Structure Designs to Active Functions. *Acc Chem Res* **55**, 1533–1545 (2022).

77. Shin, B. *et al.* Hygrobot: A self-locomotive ratcheted actuator powered by environmental humidity. *Sci Robot* **3**, eaar2629 (2018).

78. Wang, W. *et al.* Harnessing the hygroscopic and biofluorescent behaviors of genetically tractable microbial cells to design biohybrid wearables. *Sci Adv* **3**, e1601984 (2017).

79. Forterre, Y. & Dumais, J. Generating Helices in Nature. *Science* **333**, 1715–1716 (2011).

80. Rus, D. & Tolley, M. T. Design, fabrication and control of soft robots. *Nature* **521**, 467–475 (2015).

81. Siéfert, E., Reyssat, E., Bico, J. & Roman, B. Bio-inspired pneumatic shape-morphing elastomers. *Nat Mater* **18**, 24–28 (2019).

82. Melancon, D., Gorissen, B., García-Mora, C. J., Hoberman, C. & Bertoldi, K. Multistable inflatable origami structures at the metre scale. *Nature* **592**, 545–550 (2021).

83. Jones, T. J., Jambon-Puillet, E., Marthelot, J. & Brun, P. T. Bubble casting soft robotics. *Nature* **599**, 229–233 (2021).

84. Kim, H. *et al.* Shape morphing smart 3D actuator materials for micro soft robot. *Materials Today* **41**, 243–269 (2020).

85. Wang, J. & Chortos, A. Control Strategies for Soft Robot Systems. *Advanced Intelligent Systems* **4**, 2100165 (2022).

86. El-Atab, N. *et al.* Soft Actuators for Soft Robotic Applications: A Review. *Advanced Intelligent Systems* **2**, 2000128 (2020).

87. Laschi, C., Mazzolai, B. & Cianchetti, M. Soft robotics: Technologies and systems pushing the boundaries of robot abilities. *Sci Robot* **1**, eaah3690 (2016).

88. Li, M., Pal, A., Aghakhani, A., Pena-Francesch, A. & Sitti, M. Soft actuators for real-world applications. *Nat Rev Mater* **7**, 235–249 (2021).

89. Strange, M. G. *IMPLEMENTATION OF A SELF-CONTROLLING HEATER*. ntrs.nasa.gov/citations/19730015752 (1973).

90. Li, D. *et al.* Recent Advances in Electrically Driven Soft Actuators across Dimensional Scales from 2D to 3D. *Advanced Intelligent Systems* **6**, 2300070 (2024).

91. Ahn, J. *et al.* A Review of Recent Advances in Electrically Driven Polymer-Based Flexible Actuators: Smart Materials, Structures, and Their Applications. *Adv Mater Technol* **7**, 2200041 (2022).

92. Park, K., Yoon, M. K., Lee, S., Choi, J. & Thubrikar, M. Effects of electrode degradation and solvent evaporation on the performance of ionic-polymer-metal composite sensors. *Smart Mater Struct* **19**, 075002 (2010).

93. Lee, S. *et al.* Multiday operable ionic polymer-metal composites prepared using a stacking method for practical actuator applications. *Sens Actuators B Chem* **372**, 132616 (2022).

94. Guo, Y., Liu, L., Liu, Y. & Leng, J. Review of Dielectric Elastomer Actuators and Their Applications in Soft Robots. *Advanced Intelligent Systems* **3**, 2000282 (2021).

95. Suo, Z. Theory of dielectric elastomers. *Acta Mechanica Solida Sinica* **23**, 549-578 (2010).

96. Shintake, J., Schubert, B., Rosset, S., Shea, H. & Floreano, D. Variable stiffness actuator for soft robotics using dielectric elastomer and low-melting-point alloy. in *2015 IEEE/RSJ International Conference on Intelligent Robots and Systems (IROS)* 1097–1102 (IEEE, 2015). doi:10.1109/IROS.2015.7353507.

97. Sun, Y. *et al.* Origami-inspired folding assembly of dielectric elastomers for programmable soft robots. *Microsyst Nanoeng* **8**, 37 (2022).

98. Gan, J. & Zhang, X. A review of nonlinear hysteresis modeling and control of piezoelectric actuators. *AIP Adv* **9**, 040702 (2019).

99. Bertotti, Giorgio. & Mayergoyz, I. D. *The Science of Hysteresis*. (Academic Press, 2006).

100. Ahn, J. *et al.* Heterogeneous Conductance-Based Locally Shape-Morphable Soft Electrothermal Actuator. *Adv Mater Technol* **5**, 1900997 (2020).

101. Jeong, Y. *et al.* Biomimetic, Programmable, and Part-by-Part Maneuverable Single-Body Shape-Morphing Film. *Advanced Intelligent Systems* **5**, 2200293 (2023).

102. Wang, C. *et al.* Soft Ultrathin Electronics Innervated Adaptive Fully Soft Robots. *Advanced Materials* **30**, 1706695 (2018).

103. He, Q. *et al.* Electrically controlled liquid crystal elastomer–based soft tubular actuator with multimodal actuation. *Sci Adv* **5**, eaax5746 (2019).

104. Li, S. *et al.* Digital light processing of liquid crystal elastomers for self-sensing artificial muscles. *Sci Adv* **7**, eabg3677 (2021).

105. Doi, H. & Urayama, K. Thermal bending coupled with volume change in liquid crystal gels. *Soft Matter* **13**, 4341–4348 (2017).

106. Jin, B. *et al.* Programming a crystalline shape memory polymer network with thermo- and photo-reversible bonds toward a single-component soft robot. *Sci Adv* **4**, eaao3865 (2018).

107. Wu, J. *et al.* Multi-shape active composites by 3D printing of digital shape memory polymers. *Sci Rep* **6**, 24224 (2016).

108. Ge, Q., Dunn, C. K., Qi, H. J. & Dunn, M. L. Active origami by 4D printing. *Smart Mater Struct* **23**, 094007 (2014).

109. Li, J. *et al.* A biomimetic flexible fishtail embedded with shape memory alloy wires. *IEEE Access* **7**, 166906–166916 (2019).

110. Du, Y. *et al.* Dynamic characteristics of planar bending actuator embedded with shape memory alloy. *Mechatronics* **25**, 18–26 (2015).

111. Smith, C., Villanueva, A., Joshi, K., Tadesse, Y. & Priya, S. Working principle of bio-inspired shape memory alloy composite actuators. *Smart Mater Struct* **20**, 012001 (2011).

112. Lendlein, A. & Gould, O. E. C. Reprogrammable recovery and actuation behaviour of shape-memory polymers. *Nat Rev Mater* **4**, 116–133 (2019).

113. Behl, M., Kratz, K., Noechel, U., Sauter, T. & Lendlein, A. Temperature-memory polymer actuators. *Proceedings of the National Academy of Sciences* **110**, 12555–12559 (2013).

114. Min, L. *et al.* Stepless shape morphing polymer. *SmartMat* **4**, e1134 (2023).

115. Chen, L. *et al.* High-performance, low-voltage, and easy-operable bending actuator based on aligned carbon nanotube/polymer composites. *ACS Nano* **5**, 1588–1593 (2011).

116. Zeng, Z. *et al.* Low-voltage and high-performance electrothermal actuator based on

multi-walled carbon nanotube/polymer composites. *Carbon* **84**, 327–334 (2015).

117. Hu, Y., Lan, T., Wu, G., Zhu, Z. & Chen, W. A spongy graphene based bimorph actuator with ultra-large displacement towards biomimetic application. *Nanoscale* **6**, 12703–12709 (2014).

118. Meng, J. *et al.* A flexible metallic actuator using reduced graphene oxide as a multifunctional component. *Nanoscale* **9**, 12963–12968 (2017).

119. Hu, Y. *et al.* Electrically and Sunlight-Driven Actuator with Versatile Biomimetic Motions Based on Rolled Carbon Nanotube Bilayer Composite. *Adv Funct Mater* **27**, 1704388 (2017).

120. Chen, L. *et al.* Large-Deformation Curling Actuators Based on Carbon Nanotube Composite: Advanced-Structure Design and Biomimetic Application. *ACS Nano* **9**, 12189–12196 (2015).

121. Li, L. *et al.* Dual-Mechanism and Multimotion Soft Actuators Based on Commercial Plastic Film. *ACS Appl Mater Interfaces* **10**, 15122–15128 (2018).

122. Kim, H. *et al.* Biomimetic Color Changing Anisotropic Soft Actuators with Integrated Metal Nanowire Percolation Network Transparent Heaters for Soft Robotics. *Adv Funct Mater* **28**, 1801847 (2018).

123. Li, Q. *et al.* Large-strain, multiform movements from designable electrothermal actuators based on large highly anisotropic carbon nanotube sheets. *ACS Nano* **9**, 409–418 (2015).

124. Fang, Y., Pence, T. J. & Tan, X. Nonlinear elastic modeling of differential expansion in trilayer conjugated polymer actuators. *Smart Mater Struct* **17**, 065020 (2008).

125. "Nickel, Ni.", https://www.matweb.com/search/DataSheet.aspx?MatGUID=e6eb83327e534850a062dbca3bc758dc. Accessed 16 Aug. 2023.

126. Johnston, I. D., McCluskey, D. K., Tan, C. K. L. & Tracey, M. C. Mechanical characterization of bulk Sylgard 184 for microfluidics and microengineering. *Journal of Micromechanics and Microengineering* **24**, 035017 (2014).

127. Del Campo, A. & Greiner, C. SU-8: A photoresist for high-aspect-ratio and 3D submicron lithography. *Journal of Micromechanics and Microengineering* **17**, R81 (2007).

128. "VTEC PI Polyimide Parts & Shapes.", www.vtecpi.com/pdf/VtecPI.pdf. Accessed 16 Aug. 2023.

129. Müller, A., Wapler, M. C. & Wallrabe, U. A quick and accurate method to determine the Poisson's ratio and the coefficient of thermal expansion of PDMS. *Soft Matter* **15**, 779–784 (2019).

130. Chung, S. & Park, S. Effects of temperature on mechanical properties of SU-8 photoresist material. *Journal of Mechanical Science and Technology* **27**, 2701–2707

(2013).

131. Bauer, C. L. & Farris, R. J. Determination of poisson's ratio for polyimide films. *Polym Eng Sci* **29**, 1107–1110 (1989).

132. "SYLGARD^{TM} 184 Silicone Elastomer FEATURES & BENEFITS.", www.consumer.dow.com. Accessed 16 Aug. 2023.

133. Roch, I., Bidaud, P., Collard, D. & Buchaillot, L. Fabrication and characterization of an SU-8 gripper actuated by a shape memory alloy thin film. *Journal of Micromechanics and Microengineering* **13**, 330–336 (2003).

134. Gupta, M. D., Mishra, R. B., Kuriakose, I. & Hussain, A. M. Determination of thermal and mechanical properties of SU-8 using electrothermal actuators. *MRS Adv* **7**, 591–595 (2022).

135. Murphy, E. C. *et al.* Tailoring properties and processing of Sylgard 184: Curing time, adhesion, and water affinity. *J Appl Polym Sci* **137**, 48530 (2020).

136. "Overview of materials for Polyimide, Thermoset Film.", https://www.matweb.com/search/datasheet.aspx?MatGUID=0b1f084839774beaaeb6230b4ca7e06a. Accessed 16 Aug. 2023.